Three-Dimensional Imaging of Topologically Protected Strings in a Multiferroic Nanocrystal

Mansoor A. Najeeb¹, David Serban¹, Daniel G. Porter², Frank Lichtenberg³, Steve Collins², Alessandro Bombardi², Nicola A. Spaldin³, and Marcus C. Newton^{*1}

¹Department of Physics & Astronomy, University of Southampton, United Kingdom

²Diamond Light Source, Harwell Oxford Campus, Didcot, United Kingdom

³Department of Materials, ETH Zürich

Abstract 8

2

5

6

7

9

10

11

12

13

14

15

16

17

18

19

20

21 22

25

26

27

28

30

31

32

33

36

37

38

39

41

42

43

Multiferroic materials can host a plethora of intriguing phenomena due to the presence of multiple ferroic properties that break both spatial inversion symmetry and time reversal symmetry at an observable scale. Hexagonal manganite multiferroics are of particular interest as the properties of their symmetry-lowering phase transition can be described by a Mexican-hat-like potential energy surface. The early universe is proposed to have undergone a symmetry-lowering phase transition that is described by a similar Mexican-hat-like potential that gives rise to the formation of one-dimensional topologically protected defects known as cosmic strings. According to the Kibble-Zurek mechanism, hexagonal manganite multiferroics can host the crystallographic equivalent of cosmic strings and can therefore serve as a testing ground for exploration of concepts in cosmology. To date, however, direct imaging of 1D topological defects in a condensed matter material system has not been achieved. Here we report on robust three-dimensional imaging of topologically protected strings in a single hexagonal manganite nanocrystal, enabled by advances in experimental techniques. Our findings reveal multiferroic strings with a preferred phase vortex winding direction and average separation of ~93 nm.

1 Introduction 23

1.1 Universe in a Nanocrystal (Kibble-Zurek Mechanism)

Multiferroic materials are single-phase materials where two or more ferroic properties including ferromagnetism, ferroelectricity, ferroelasticity or ferrotoroidicity co-exist. 1-5 Hexagonal manganites (h- $RMnO_3$), where $R \in \{Y, Dy, Er, (or a small rare-earth ion)\}$, are multiferroic materials where ferroelectric ordering arises due to tilting of MnO₅ bipyramids and buckling of R³⁺ ions along the c-axis direction, i.e. improper geometric ferroelectricity (Fig. 1a). Tilting occurs collectively either toward or away from a central R³⁺ ion positioned at either of three distinct lattice sites $(\alpha, \beta \text{ or } \gamma)$ leading to six symmetryequivalent trimerisation states (Fig. 1b). The potential energy surface that describes the ferroelectric phase transition therefore has a Mexican-hat-like topology (Fig. 1c) where the radial distance from the central peak represents the magnitude of MnO₅ bipyramid tilting and the six equivalent minima in the Z₆-symmetry brim represent the symmetry-equivalent trimerisation ground states. This potential has similar symmetry to the ' ϕ^4 ' potential that describes the formation of the Higgs boson⁶⁻⁸ as well as one-dimensional topological defects such as the cosmic strings, proposed to have formed in the early universe. As a result, hexagonal manganites can host the crystallographic equivalent of cosmic strings in the form of topologically protected vortex strings at the intersection of ferroelectric domains (Fig. 1d). When coupled with the Zurek mechanism, which is used to estimate the defect number density (n) as a function of the rate of quenching across the ferroelectric phase transition, the Kibble-Zurek mechanism (KZM) is able to describe a phase transition in any system with the required symmetry properties. 9,10 The KZM is therefore generally applicable in such cases and determines the defect number density, nas:

^{*}M.C.Newton@soton.ac.uk

$$n \approx \frac{1}{\xi_0^{D-d}} \left(\frac{\tau_0}{\tau_q}\right)^{(D-d)\nu/(1+z\nu)} \tag{1}$$

where ξ_0 is the zero-temperature correlation length, $\tau_0=\xi_0/c$ is the zero-temperature time, c is the speed at which information is transferred in the system, τ_q is the quench time, D, d are the dimensions of the space and defect respectively and ν , z are critical exponents that are determined by the universality class of the system. For a particular material and universality class, scaling of the defect number density n is therefore determined solely by the quenching rate. Varying the rate of cooling through a ferroelectric phase transition becomes equivalent to varying the rate of early universe expansion. To date, however, non-destructive three-dimensional imaging of 1D topological defects in materials has proven challenging.

1.2 Bragg CDI Synopsis

Bragg coherent diffraction imaging (BCDI) is a particularly powerful tool for the study of multiferroics at the nanoscale as it is able to reveal the ferroelectric domain structure in three dimensions. ^{18–20} BCDI is performed by illuminating a nanoscale crystal in the Bragg reflection geometry with a spatially coherent x-ray source, so that the coherence length exceeds the dimensions of the nanocrystal. The resulting scattered light from the nanocrystal interferes in the far-field, producing a three-dimensional reciprocal-space diffraction pattern. ^{21–24} The diffracted intensity is measured using a photon counting area detector which is optimally positioned to resolve the finest fringes of the diffraction pattern. The third dimension of the diffraction pattern is obtained by rotating the crystal through the Bragg condition while maintaining a largely fixed incident angle (a rocking-curve measurement).

Iterative phase reconstruction methods are then used to recover the complex three-dimensional electron density and phase information present within the x-rays that is acquired when coherently scattered from the nanocrystal. The displacement of ions throughout the bulk is directly related to the recovered phase and can be used to obtain strain information according to the relation $\phi = \mathbf{Q} \cdot \mathbf{u}$, where \mathbf{u} is the atomic displacement from the equilibrium lattice position. Diffraction patterns from multiple Bragg reflections of a single nanocrystal are combined to recover the full displacement field and its spatial derivative which is the strain tensor field. 25,27

1.3 Summary of Manuscript

Here we utilise BCDI to directly image in three-dimensions topologically protected strings in a single hexagonal manganite nanocrystal.

2 Results

2.1 Multiple Bragg Peak Experiment

Nanocrystals of hexagonal dysprosium manganite (h-DyMnO $_3$) were prepared from bulk melt-grown h-DyMnO $_3$ as described in the Methods section. Laboratory based x-ray diffraction experiments were used to verify the correct hexagonal crystallographic phase was obtained with lattice parameters $a=b=6.18\,\text{Å}$ and $c=11.4\,\text{Å}$. The ferroelectric domain structure in h-DyMnO $_3$ is formed upon cooling the high symmetry paraelectric phase (P63/mmc) through the critical temperature (T $_c$) of \sim 1200 K to the lower symmetry ferroelectric phase (P63cm). In this case, quenching was performed at a cooling rate of \sim 1000 K per second.

BCDI experiments were performed in air on beamline I16 of the Diamond Light Source synchrotron facility using 9 keV x-rays and a quad Merlin detector 31 where each pixel measured 55 μ m \times 55 μ m. The sample-to-detector distance during measurements was fixed at 1.31 meters. The full beam x-ray flux at the sample was 3 \times 10 13 photons s⁻¹. Samples containing mono-dispersed h-DyMnO₃ nanocrystals were mounted at the eucentric point of the 6-axis kappa diffractometer. The beam size was reduced down to 50 \times 50 μ m² using front-end slits. A single specular Bragg reflection corresponding to the $G_{(110)}$ reciprocal lattice plane from a single h-DyMnO₃ nanocrystal was located and its three-dimensional diffraction pattern recorded. Additionally, the (111) Bragg reflection from the same nanocrystal was

found by first rotating the experimental geometry (\mathbf{Q} -vector) through the cone of all possible points where $\mathbf{Q} \cdot \mathbf{Q}_{(110)} = \mathbf{G}_{(111)} \cdot \mathbf{G}_{(110)}$. Subsequently, the (112) Bragg reflection from the same nanocrystal was found by defining an orientation matrix using the location of the previous two reflections. Each diffraction speckle pattern was subsequently coordinate transformed into Cartesian coordinates and sampled onto a regular grid in preparation for concurrent phase retrieval.

2.2 BCDI Concurrent Phase Retrieval

Phase reconstruction of the real-space electron density and displacement field $\mathbf{u}(\mathbf{r})$ was performed concurrently^{20,25,32-34} using the *Interactive Phase Retrieval Suite*³⁵ for all three Bragg reflections of a single nanocrystal. Concurrent phase retrieval was previously shown to provide stronger convergence and high reproducibility than independent phase retrieval due to inherent redundancy in the concurrent approach.²⁵ Phase reconstruction consisted of repeated cycles of 5000 iterations of Fienup's Hybrid Input-Output (HIO) algorithm with a masked diffraction pattern followed by 100 iterations of the Error Reduction (ER) algorithm.³⁶ In each case, a support (solvent) was employed that was created using a manual version of the shrink-wrap method.^{27,37} Phase retrieval attempts were repeated at least three times with a revised shrink-wrapped support from the previous attempt until no appreciable changes were observed in the support morphology between reconstruction attempts.

2.3 BCDI of Ferroelectric Phase Vortices

Figure 2 shows the reconstructed real-space electron density map of the single h-DyMnO $_3$ nanocrystal for each of the three Bragg reflections. In addition, the phase information at the corresponding location is mapped onto the surface. Considerable variation in the phase information across the surface is observed in each reflection with the (111) reflection clearly showing striped phase patterns across the surface. Each reconstruction shows consistency in the morphology of the nanocrystals confirming good agreement in the reconstruction process. The morphology is shown at a 95% isosurface with nominal dimensions of 1.22 μ m in width and 2.07 μ m in height. Real-space electron density maps without phase information mapped onto the surface are shown in the Supplementary Materials. The resolution for each reconstruction was estimated using the Phase Retrieval Transfer Function (PRTF)³⁸ and was determined to be 35.2 nm, 46.7 nm and 20.8 nm for the (110), (111) and (112) Bragg reflections respectively (Fig. S6 of Supplementary Material).

Figure 3 shows slices through the reconstructed electron density map of the (111) reflection normal to the x-axis (\bf{a}), y-axis (\bf{b}) and z-axis (\bf{c}) respectively. Slices are shown at five 100 nm intervals for each orientation. Equivalent plots for the (110) and (112) reflections are found in the Supplementary Material. Stripe domain structure (\bf{a}) and a number of ferroelectric vortex patterns (\bf{b} and \bf{c}) are visible throughout the nanocrystal volume, primarily in the (111) reflection phase information. Vortex cores appear with a preferred winding direction for the phase information that surrounds the defect, in the plane of view. In Fig. 3(\bf{b}) this corresponds to a positive increase in phase for anti-clockwise winding direction. From the observation of vortex cores with a preferred winding direction, we can infer that the topologically protected strings within the nanocrystal are not winding back to one another as this would produce vortex cores with opposite winding direction - which are not observed. Vortex cores are nominally separated by 93 nm (see Fig. 5 \bf{g}), with separations up to 120 nm observed, as shown. Phase paths connecting pairs of vortex cores are also observed, most clearly in Fig. 3(\bf{c}).

Figure 4 shows the strain tensor information ε which is the spatial derivative of the displacement field, defined as $\varepsilon = (1/2) \{ \nabla \mathbf{u} + (\nabla \mathbf{u})^T \}$. Cross-sections through each of the six independent strain tensor components normal to the x-axis direction are shown in each column where each slice is taken at locations shown in Fig. 3. Cross-sections normal to the y-axis direction and z-axis direction are shown in the supplementary material. Strain information with patches of tensile and compressive strain are visible in all components except the ε_{zz} component which is largely strain free in contrast. A likely cause of this effect relates to the uniformity of displacements along the c-axis direction, for which there is a significant component in the z-axis direction. Crucially surface effects such as oxygen depletion, which would appear as strain layers near to the surface, are not observed in the strain tensor information suggesting that h-DyMnO₃ nanocrystals were synthesised with sufficiently high phase purity for such effects not to be visible at the resolution of this measurement.

Figure 5 shows topologically protected strings defined as the path for each vortex core in the phase map information for the (111) reflection electron density map of Fig. 3. The (111) reflection was chosen as the strings were more clearly observed in the phase information when compared to phase information in the (110) and (112) reflection density maps. The accompanying Supplementary Video shows a three-dimensional animation of the topologically protected strings to facilitate with visualisation. Slices through the reconstructed h-DyMnO₃ nanocrystal phase information maps are shown in Fig. 5a and Fig. 5d along with the coincidence points of the strings with phase vortex cores. Strings pass through the h-DyMnO₃ nanocrystal unperturbed by the surface and in some places appear to fold back on themselves to form loops. In order to determine the density of topologically protected strings within the nanocrystal we defined the Path Distribution Function (PthDF), g(r), which describes the distribution of minimum distances between pairs of strings within the nanocrystal volume. This is analogous to the Pair Distribution Function (PDF)³⁹⁻⁴¹ with the exception that it operates on one-dimensional paths as opposed to zero-dimensional points. The PthDF is defined as:

$$g(r) = \sum_{i} \sum_{j \neq i} \int dt \, \rho_i(t) \, \delta(s_{ij}(t) - r) , \qquad (2a)$$

$$s_{ij}(t) = \min \left\{ \xi_{ij}(t, t') \mid t' \in \mathbb{R} \land \gamma_i(t') \in \mathcal{N} \right\} , \qquad (2b)$$

$$\xi_{ij}(t,t') = \|\boldsymbol{\gamma}_i(t) - \boldsymbol{\gamma}_j(t')\| \tag{2c}$$

where $\gamma_i(t)$ are the coordinates of a point on the multiferroic string trajectory with index i and density $\rho_i(t)$, while \mathcal{N} are the set of all points within the nanocrystal volume. Figure 5**g** shows the resulting PthDF for multiferroic strings in the (111) phase map. It shows a clear preference for strings to separate by \sim 93 nm. The corresponding area density of strings, (n), is estimated from the preferred string separation and found to agree with those previously reported for the same cooling rate in bulk samples. From this we can infer that there are likely no fundamental changes in domain structure between our nanoscale structure and bulk samples.

3 Discussion 161

Earlier studies aimed at revealing three-dimensional domains, domain walls, and multiferroic strings have employed destructive means such as sequential Focussed Ion Beam (FIB) cutting of cross-sections of bulk multiferroic materials. Subsequent imaging of these slices was performed using either Scanning Electron Microscopy (SEM), piezoresponse force microscopy (PFM) or conductive atomic force microscopy (cAFM). The resulting images were used to successfully reveal domain and domain wall contrast. 13,43 SEM, PFM and cAFM measurements however were unable to reveal the winding direction of the vortex structure, which is readily observed when using Bragg CDI. While the robust nature of topologically protected structure lends itself to destructive mapping and imaging techniques, such measurements have the disadvantage of lacking repeatability. Bragg CDI however offers non-destructive imaging where measurements can be repeated on the same sample provided the dimensions of the material are below the coherence volume of the coherent x-ray probe. 44 When this isn't the case, alternative and more challenging approaches such as Bragg ptychography can in principle provide equivalent information.⁴⁵ Hexagonal manganite multiferroics often contain dense elements such as dysprosium that can produce dynamical scattering effects. While in principle this may influence the BCDI phase reconstruction process, dynamical scattering effects are often found to be less significant than refraction and absorption effects and therefore generally do not warrant further consideration. 46-48

Bragg CDI also provides strain information and has revealed in this study that strings, which are lines of the paraelectric phase trapped in the ferroelectric structure, induce tensile and compressive strain of up to 0.1 along commensurate paths, with magnitude exceeding that of strain within the broader domain regions. Future BCDI studies on multiferroic strings where the effect of strain is studied dynamically, via progressive deformation,⁴⁹ could provide further insight into the role of strain in the formation of multiferroic strings.

In summary, we have demonstrated three-dimensional imaging of predicted one-dimensional topologically protected strings in a single nanocrystal of multiferroic hexagonal manganite h-DyMnO₃. The

density of the strings matches that inferred from surface measurements of bulk samples prepared at similar quenching rates. In addition, phase map information reveals that phase vortex structures, whose core locations define the path of each string, appear with a preferred winding direction and separation.

Our findings indicate the promise of lens-less imaging techniques such as Bragg CDI for the study of three-dimensional structure and properties of topologically protected defects in materials. Possible other areas of application include monopoles, strings and textures in liquid crystals, dislocations in metals and polar skyrmions in ferroelectrics. We hope that the results presented here inspire further work in these directions.

4 Methods

4.1 Synthesis and Quenching of DyMnO₃ Nanocrystals

Bulk DyMnO₃ usually crystallises into a perovskite structure. However, when the composition

$$\frac{1}{2} Dy_2 O_3 + \frac{1}{2} Mn_2 O_3 = DyMnO_3$$

is melted and crystallised under argon, some oxygen is released resulting in an oxygen-deficient composition DyMnO $_{3-\delta}$ (1 >> δ > 0) which adopts a hexagonal YMnO $_3$ type structure. This structure is denoted as h-DyMnO $_3$.

Bulk melt-grown h-DyMnO $_3$ single crystals were mechanically ground in to a fine nanocrystalline powder and transferred to a ceramic boat for annealing. The annealing was carried out under vacuum at 1000 degrees Celsius for 10 minutes. After the annealing period was complete, in-vacuum manipulation was used to swiftly translate the ceramic boat into the room temperature portion of the vacuum furnace thus inducing rapid quenching, at \sim 1000 K/s, of the annealed nanocrystals. The h-DyMnO $_3$ nanocrystal powder was subsequently dispersed in isopropanol and sonicated for 15 minutes to ensure uniform dispersion. Following sedimentation of the heavier nanocrystals, the supernatant solution from the upper layer was carefully pipetted and drop-casted on to a cleaned Silicon (100) substrate to form a thin layer of mono-dispersed h-DyMnO $_3$ nanocrystals.

5 Acknowledgements

This work was supported by UK Research and Innovation (UKRI) grant MR/T019638/1 for the University of Southampton Department of Physics & Astronomy and the ETH Zürich. We acknowledge Diamond Light Source for the provision of time on Beamline I16 under Proposal MM34302-1.

6 Author Contributions

M.C.N. wrote the manuscript with input from all authors. M.C.N. designed and supervised the study. F.L. prepared and supplied the bulk samples. M.A.N. synthesized the nanocrystals. M.A.N., D.S., D.G.P., S.P.C., A.B. and M.C.N. contributed to the BCDI experiment at Diamond Light Source. M.C.N. performed data reconstruction and analysis. N.A.S. provided theoretical interpretation of the ferroelectric domain structure and topology.

7 Data Availability

The data underpinning the findings of this study are available from M.C.N. upon reasonable request.

8 Code Availability

The computational analysis in this study utilised 'Bonsu: The Interactive Phase Retrieval Suite' software package for data preparation and concurrent phase retrieval algorithms. It can be downloaded through PyPI (https://pypi.org/project/Bonsu/) or GitHub (https://github.com/bonsudev/bonsu). This software

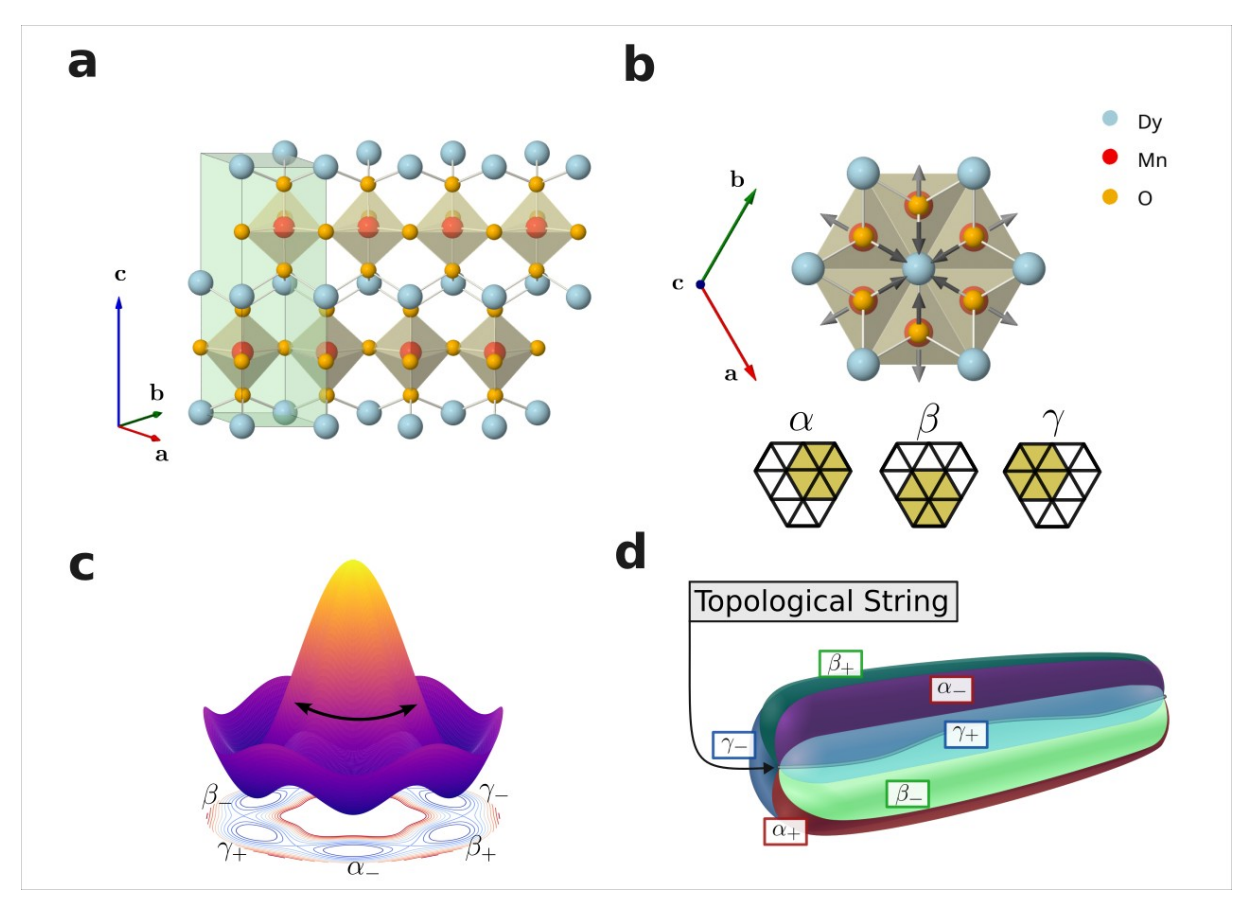


Figure 1: a, Illustration of the crystal structure of h-DyMnO₃ in the paraelectric phase, shown with 4×1 unit cells. A single unit cell is highlighted by the shaded green region. **b**, Crystal structure of the centrosymmetric paraelectric phase of h-DyMnO₃ projected normal to the c-axis. Arrows indicate the resulting displacement of oxygen ions due to tilting of MnO₅ polyhedra during the trimerisation transition into the low temperature ferroelectric phase. Tilting occurs collectively either toward (+) or away (-) from one of the central dysprosium ions $(\alpha, \beta \text{ or } \gamma)$ leading to six symmetry-equivalent trimerisation states corresponding to the six equivalent minima of the Mexican-hat-like potential energy surface (c). Each minimum in **c** corresponds to the ferroelectric phase while the high symmetry paraelectric phase is represented by the central peak. d, Illustration of three-dimensional topological domains forming a vortex (front) - antivortex (back) pair connected by a topologically protected string.

is integral to the research and is made available to ensure transparency and reproducibility in scientific research.

225

226

228

229

230

232

235

References 227

- [1] Schmid, H. Multi-ferroic magnetoelectrics. Ferroelectrics **162**, 317–338 (1994).
- [2] Fiebig, M., Lottermoser, T., Meier, D. & Trassin, M. The evolution of multiferroics. Nature Reviews Materials **1**, 16046 (2016).
- [3] Cheong, S.-W. & Mostovoy, M. Multiferroics: a magnetic twist for ferroelectricity. Nature Materials 231 **6**, 13–20 (2007).
- [4] Spaldin, N. A. & Fiebig, M. The renaissance of magnetoelectric multiferroics. Science 309, 391 -233 392 (2005). 234
- [5] Multiferroics march on. Nature Materials 18, 187–187 (2019).
- [6] Higgs, P. W. Broken symmetries and the masses of gauge bosons. Phys. Rev. Lett. 13, 508-509 236 (1964).237

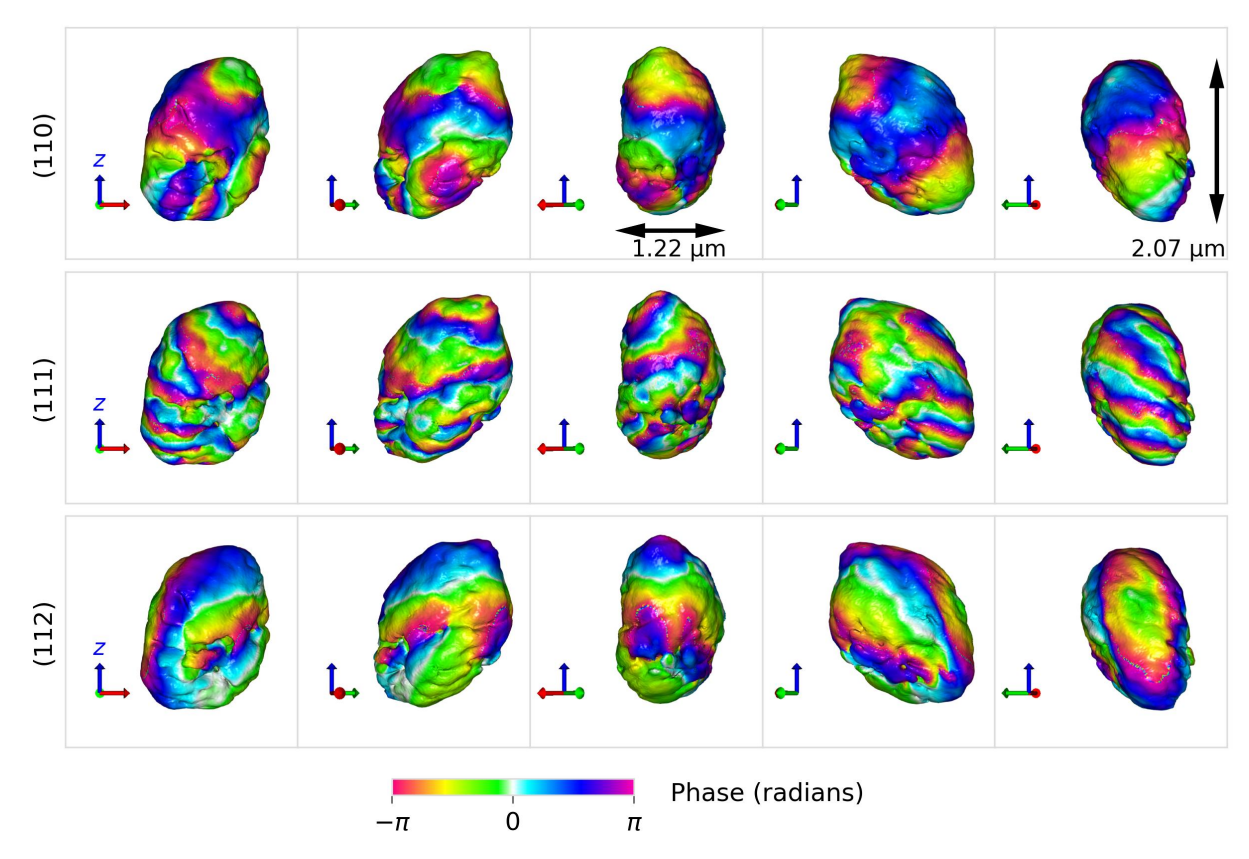


Figure 2: Concurrent BCDI reconstruction of the morphology of a single h-DyMnO₃ nanocrystal showing phase information mapped onto the surface of the crystals. Each of the 5 frames per row, from left to right, differs by a rotation of 72 degrees normal to the vertical z-axis direction as defined in the image. Multiple stripe phase patterns are visible predominantly in the (111) reflection of the nanocrystal.

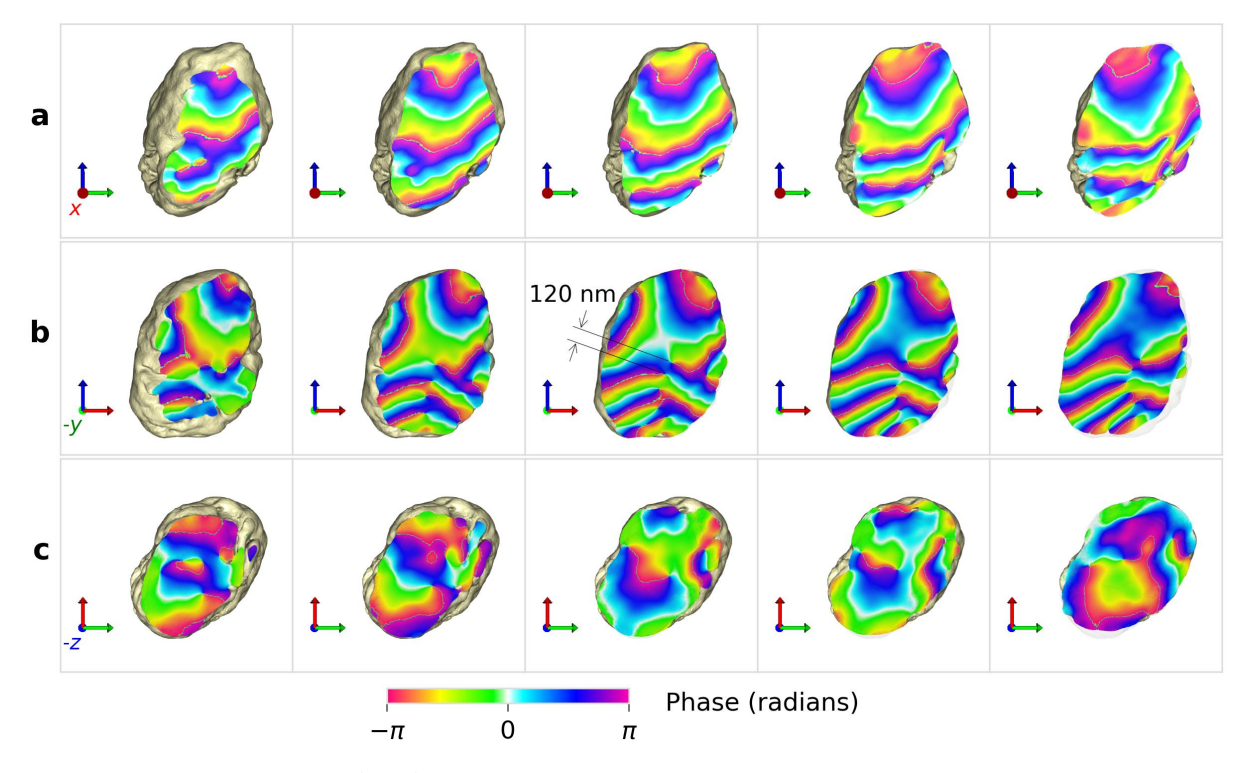


Figure 3: Slices through the (111) reflection of the reconstructed h-DyMnO $_3$ nanocrystal shown for three orthogonal projections. The x, -y and -z unit vector points out of the image plane in the row labelled $\bf a$, $\bf b$ and $\bf c$ respectively. Slices are taken at 100 nm intervals directed normal to the image plane. Numerous vortex structures are visible in the phase information and appear with a preferred winding direction. Central image on row $\bf b$ labels two vortex cores separated by 120 nm.

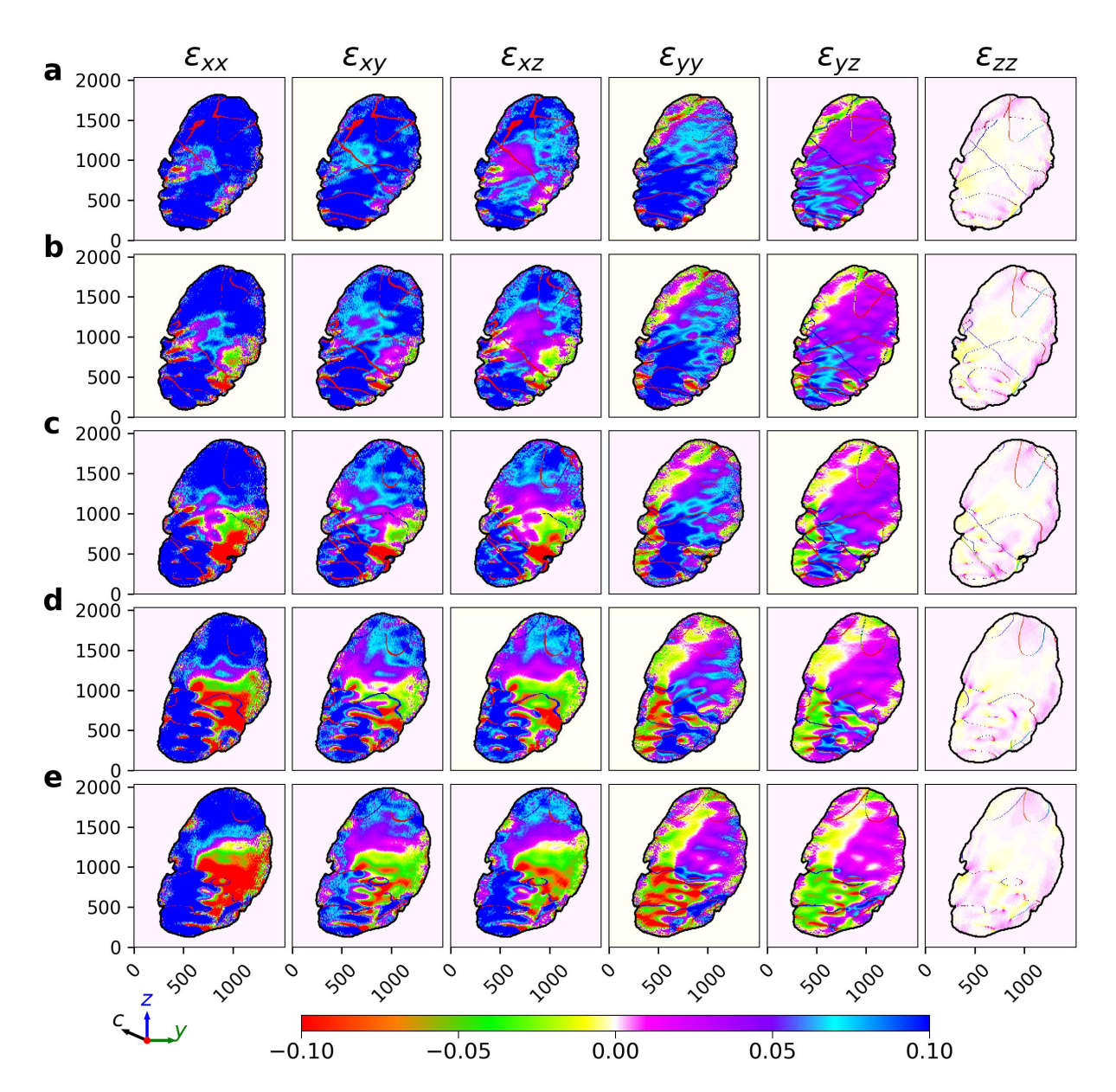


Figure 4: Strain tensor components of the reconstructed h-DyMnO $_3$ nanocrystal. Six independent components of the strain tensor are shown in each column. Cross-sectional planes taken at the same locations shown in Fig. 3, are shown in each row. Axes have units of nanometers.

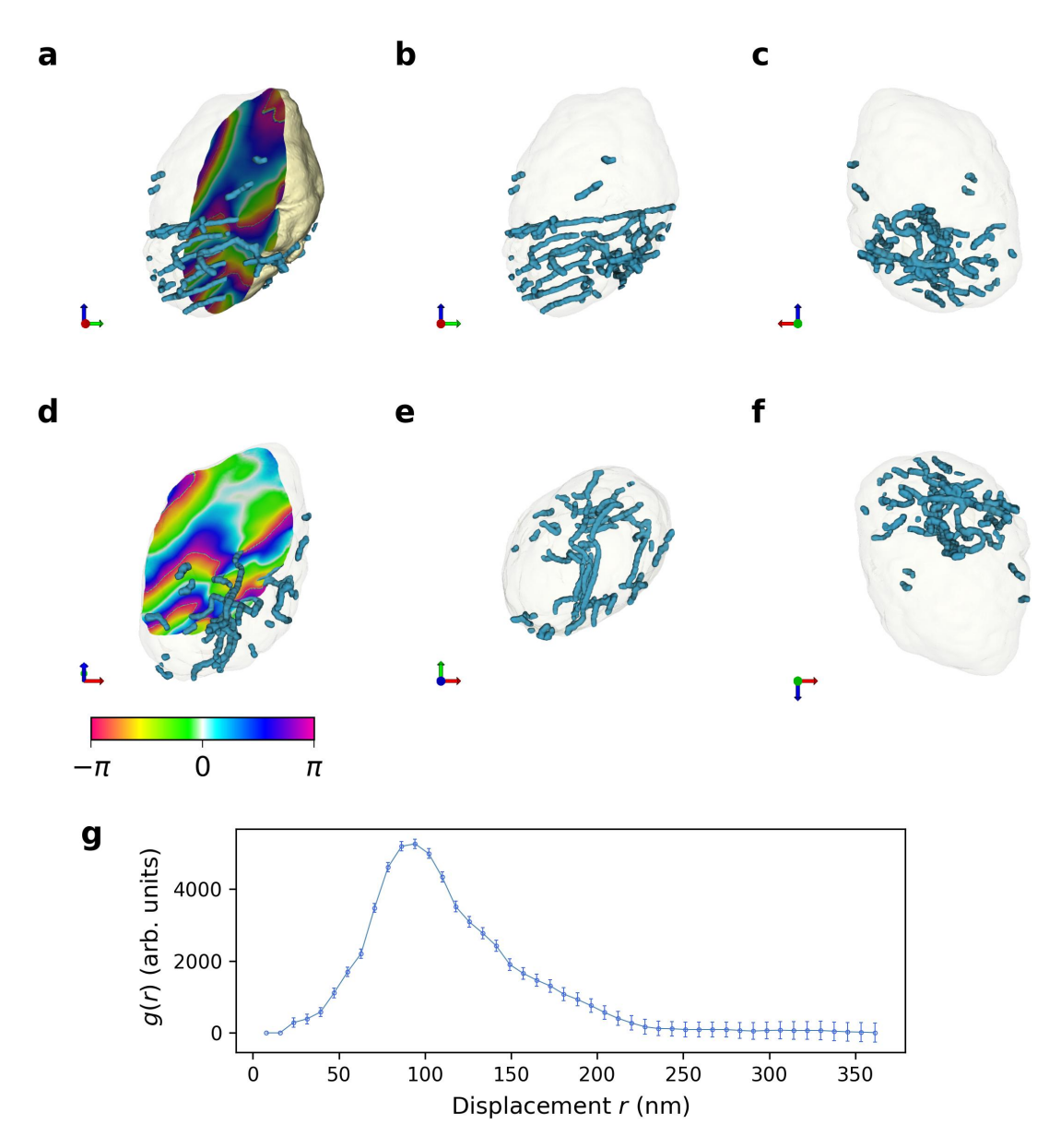


Figure 5: Three-dimensional images of topologically protected strings defined as the path of each vortex core for the (111) reflection throughout the reconstructed h-DyMnO $_3$ nanocrystal . **a**, Slice through the reconstructed h-DyMnO $_3$ nanocrystal showing coincidence points of strings with vortex cores. **b**, Strings shown with identical orientation as shown in (**a**). **c**, Reoriented view of strings. **d**, Alternative view of a slice through the reconstructed h-DyMnO $_3$ nanocrystal showing coincidence points of topological strings with vortex cores. **e**, Strings shown with identical orientation as shown in (**d**). **f**, Reoriented view of topological strings. **g**, Path Distribution Function (PthDF), g(r), which describes the distribution of distances between pairs of strings, independent of orientation. Error bars are twice the standard deviation.

[7] Goldstone, J. Field theories with « superconductor » solutions. Il Nuovo Cimento (1955-1965) 19. 154-164 (1961).

239

244

245

246

249

250

251

252

253

256

258

259

260

262

263

264

266

267

269

270

271

272

273

277

278

279

280

281

- [8] Tumasyan, A. et al. A portrait of the higgs boson by the cms experiment ten years after the discovery. Nature **607**, 60-68 (2022).
- [9] Kibble, T. W. B. Topology of cosmic domains and strings. Journal of Physics A: Mathematical and 242 General **9**, 1387 (1976). 243
- [10] Zurek, W. H. Cosmological experiments in superfluid helium? *Nature* **317**, 505–508 (1985).
- [11] del Campo, A. & Zurek, W. H. Universality of phase transition dynamics: Topological defects from symmetry breaking. International Journal of Modern Physics A 29, 1430018 (2014). URL https: //doi.org/10.1142/S0217751X1430018X. https://doi.org/10.1142/S0217751X1430018X.
- [12] Lin, S.-Z. et al. Topological defects as relics of emergent continuous symmetry and higgs condensation of disorder in ferroelectrics. Nature Physics 10, 970–977 (2014). URL https://doi.org/10. 1038/nphys3142.
- [13] Meier, Q. N. et al. Global formation of topological defects in the multiferroic hexagonal manganites. Phys. Rev. X 7, 041014 (2017).
- [14] Spaldin, N. A. Multiferroics: from the cosmically large to the subatomically small. *Nature Reviews* Materials 2, 17017 EP - (2017). Comment.
- [15] Meier, Q. N. et al. Manifestation of structural higgs and goldstone modes in the hexagonal manganites. Phys. Rev. B 102, 014102 (2020).
- [16] Du, K. et al. Kibble-zurek mechanism of ising domains. Nature Physics 19, 1495–1501 (2023). URL 257 https://doi.org/10.1038/s41567-023-02112-5.
- [17] Antunes, N. D., Bettencourt, L. M. A. & Zurek, W. H. Vortex string formation in a 3d u(1) temperature quench. Phys. Rev. Lett. 82, 2824–2827 (1999). URL https://link.aps.org/doi/10.1103/PhysRevLett. 82.2824.
- [18] Karpov, D. et al. Three-dimensional imaging of vortex structure in a ferroelectric nanoparticle driven by an electric field. Nature Communications 8, 280 (2017). URL https://doi.org/10.1038/ s41467-017-00318-9.
- [19] Diao, J. et al. Evolution of ferroelastic domain walls during phase transitions in barium titanate nanoparticles. Phys. Rev. Mater. 4, 106001 (2020). URL https://link.aps.org/doi/10.1103/ PhysRevMaterials.4.106001.
- [20] Mokhtar, A. H. et al. Three-dimensional domain identification in a single hexagonal manganite nanocrystal. Nature Communications 15, 3587 (2024).
- [21] von Laue, M. Dieäußere Form der Kristalle in ihrem Einfluß auf die Interferenzerscheinungen an Raumgittern. Annalen der Physik 26, 55-85 (1936).
- [22] Miao, J., Kirz, J. & Sayre, D. The oversampling phasing method. Acta Crystallographica Section D 56, 1312-1315 (2000).
- [23] Pfeifer, M., Williams, G., Vartanyants, I., Harder, R. & Robinson, I. Three-dimensional mapping of a deformation field inside a nanocrystal. Nature 442, 63-66 (2006).
- [24] Robinson, I. & Miao, J. Three-dimensional coherent x-ray diffraction microscopy. MRS Bulletin 29, 276 177-181 (2004).
- [25] Newton, M. C. Concurrent phase retrieval for imaging strain in nanocrystals. Phys. Rev. B 102, 014104 (2020).
- [26] Robinson, I. & Harder, R. Coherent x-ray diffraction imaging of strain at the nanoscale. Nature Materials 8, 291-298 (2009).

[27] Newton, M. C., Leake, S. J., Harder, R. & Robinson, I. K. Three-dimensional imaging of strain in a single zno nanorod. *Nature Materials* **9**, 120–124 (2010).

- [28] Lichtenberg, F. et al. Melt-grown synthesis of oxide materials by the floating zone method: Presentation of a custom-made data and image recording, processing, and visualization system for a cyberstar mirror furnace. ETH Zurich (2021). URL https://doi.org/10.3929/ethz-b-000493880. The synthesis of melt-grown hexagonal DyMnO $_{3-\delta}$ is presented in part 3.3.
- [29] Lichtenberg, F., Lilienblum, M., Batlogg, B., Spaldin, N. & Fiebig, M. Synthesis of melt-grown hexagonal YMnO $_3$, YMn $_{0.95}$ O $_{2.93}$, YMnO $_{3+y}$, and DyMnO $_{3-\delta}$ and study of their properties by powder x-ray diffraction, piezoresponse force microscopy, a squid magnetometer, and thermogravimetry. *ETH Zurich* (2019). URL https://doi.org/10.3929/ethz-b-000357996.
- [30] Harikrishnan, S. et al. Phase transitions and rare-earth magnetism in hexagonal and orthorhombic dymno3 single crystals. *Journal of Physics: Condensed Matter* **21**, 096002 (2009).
- [31] Plackett, R. et al. Merlin: a fast versatile readout system for medipix3. Journal of Instrumentation **8**, C01038 (2013). URL https://dx.doi.org/10.1088/1748-0221/8/01/C01038.
- [32] Wilkin, M. J. et al. Experimental demonstration of coupled multi-peak bragg coherent diffraction imaging with genetic algorithms. *Phys. Rev. B* **103**, 214103 (2021).
- [33] Gao, Y., Huang, X., Yan, H. & Williams, G. J. Bragg coherent diffraction imaging by simultaneous reconstruction of multiple diffraction peaks. *Phys. Rev. B* **103**, 014102 (2021).
- [34] Maddali, S. et al. Concurrent multi-peak bragg coherent x-ray diffraction imaging of 3d nanocrystal lattice displacement via global optimization. npj Computational Materials **9**, 77 (2023).
- [35] Newton, M. C., Nishino, Y. & Robinson, I. K. *Bonsu*: the interactive phase retrieval suite. *Journal of Applied Crystallography* **45**, 840–843 (2012).
- [36] Fienup, J. R. Phase retrieval algorithms: a comparison. Appl. Opt. 21, 2758-2769 (1982).
- [37] Marchesini, S. et al. X-ray image reconstruction from a diffraction pattern alone. *Phys. Rev. B* **68**, 140101 (2003).
- [38] Chapman, H. N. et al. High-resolution ab initio three-dimensional x-ray diffraction microscopy. J. Opt. Soc. Am. A 23, 1179–1200 (2006).
- [39] Billinge, S. J. L. The rise of the x-ray atomic pair distribution function method: a series of fortunate events. *Philosophical Transactions of the Royal Society A: Mathematical, Physical and Engineering Sciences* **377**, 20180413 (2019). URL https://royalsocietypublishing.org/doi/abs/10.1098/rsta.2018. 0413. https://royalsocietypublishing.org/doi/pdf/10.1098/rsta.2018.0413.
- [40] del Campo, A., Gómez-Ruiz, F. J. & Zhang, H.-Q. Locality of spontaneous symmetry breaking and universal spacing distribution of topological defects formed across a phase transition. *Phys. Rev. B* **106**, L140101 (2022). URL https://link.aps.org/doi/10.1103/PhysRevB.106.L140101.
- [41] Thudiyangal, M. & del Campo, A. Universal vortex statistics and stochastic geometry of bose-einstein condensation. *Phys. Rev. Res.* **6**, 033152 (2024). URL https://link.aps.org/doi/10.1103/PhysRevResearch.6.033152.
- [42] Griffin, S. M. et al. Scaling behavior and beyond equilibrium in the hexagonal manganites. *Phys. Rev.* X **2**, 041022 (2012).
- [43] Roede, E. D. *et al.* The third dimension of ferroelectric domain walls. *Advanced Materials* **34**, 2202614 (2022). URL https://onlinelibrary.wiley.com/doi/abs/10.1002/adma.202202614. https://onlinelibrary.wiley.com/doi/pdf/10.1002/adma.202202614.
- [44] Leake, S. J., Newton, M. C., Harder, R. & Robinson, I. K. Longitudinal coherence function in x-ray imaging of crystals. *Opt. Express* **17**, 15853–15859 (2009). URL https://opg.optica.org/oe/abstract. cfm?URI=oe-17-18-15853.

[45] Hruszkewycz, S. O. et al. High-resolution three-dimensional structural microscopy by singleangle bragg ptychography. Nature Materials 16, 244-251 (2017). URL https://doi.org/10.1038/ nmat4798.

328

329

331

332

333

334

335

340

- [46] Shabalin, A. G., Yefanov, O. M., Nosik, V. L., Bushuev, V. A. & Vartanyants, I. A. Dynamical effects 330 in bragg coherent x-ray diffraction imaging of finite crystals. Phys. Rev. B 96, 064111 (2017). URL https://link.aps.org/doi/10.1103/PhysRevB.96.064111.
- [47] Gao, Y. et al. Modeling and experimental validation of dynamical effects in bragg coherent x-ray diffractive imaging of finite crystals. Phys. Rev. B 106, 184111 (2022). URL https://link.aps.org/doi/ 10.1103/PhysRevB.106.184111.
- [48] Authier, A. Dynamical Theory of X-Ray Diffraction (Oxford University Press, 2003). URL https://doi. 336 org/10.1093/acprof:oso/9780198528920.001.0001. 337
- [49] Newton, M. C., Shi, X., Wagner, U. & Rau, C. Coherent diffraction imaging of a progressively deformed nanocrystal. Phys. Rev. Mater. 3, 043803 (2019). URL https://link.aps.org/doi/10.1103/ PhysRevMaterials.3.043803.